A&A 654, A149 (2021)
https://doi.org/10.1051/0004-6361/202141425

Astronomy & Astrophysics

Electron conduction opacities at the transition between moderate and strong degeneracy: Uncertainties and impacts on stellar models

Santi Cassisi[1,2], Alexander Y. Potekhin[3], Maurizio Salaris[4], and Adriano Pietrinferni[1]

[1] INAF-Osservatorio Astronomico d'Abruzzo, via M. Maggini, sn. 64100, Teramo, Italy
e-mail: santi.cassisi@inaf.it
[2] INFN – Sezione di Pisa, Largo Pontecorvo 3, 56127 Pisa, Italy
[3] Ioffe Institute, Politekhnicheskaya 26, Saint Petersburg 194021, Russia
[4] Astrophysics Research Institute, Liverpool John Moores University, IC2, Liverpool Science Park, 146 Brownlow Hill, Liverpool L3 5RF, UK

Received 29 May 2021 / Accepted 25 August 2021

ABSTRACT

Electron conduction opacities are one of the main physics inputs for the calculation of low- and intermediate-mass stellar models. A critical question considers how to devise a bridge when calculating both moderate and strong degeneracy, which are necessarily performed adopting different methods. The density-temperature regime at the boundary between moderate and strong degeneracy is, in fact, crucial for modelling the helium cores of red giant branch stars and the hydrogen-helium envelopes of white dwarfs. Prompted by newly published, improved calculations of electron thermal conductivities and opacities for moderate degeneracy, we study different, physically motivated prescriptions to bridge these new computations with well-established results in the regime of strong degeneracy. We find that these varied prescriptions have a sizable impact on the predicted He-core masses at the He-flash (up to 0.01 $M_{\odot}$ for initial total masses far from the transition to non-degenerate He-cores and up to ∼0.04 $M_{\odot}$ for masses around the transition), the tip of the red giant branch (up to ∼0.1 mag), and the zero-age horizontal branch luminosities (up to 0.03 dex for masses far from the transition and up to ∼0.2 dex around the transition), and white dwarf cooling times (up to 40–45% at high luminosities, and up to ∼25% at low luminosities). Current empirical constraints on the tip of the red giant branch and the zero age horizontal branch absolute magnitudes do not yet allow for the definitive exclusion of any of these alternative options for the conductive opacities. Tests against observations of slowly-cooling faint WDs in old stellar populations will need to be performed to see whether they are capable of setting some more stringent constraints on bridging calculations of conductive opacities for moderate and strong degeneracy.

Key words. opacity – stars: interiors – stars: late-type – stars: low-mass – white dwarfs

1. Introduction

Calculations of the thermal conductivity for degenerate electrons and the corresponding electron conduction opacities are a crucial input in the calculations involved in stellar evolution models. When electron degeneracy sets in the stellar interiors, electron conduction becomes the dominant energy transport mechanism and the values of the electron conduction opacities are critical for the accurate calculation of the models' thermal stratification (see, e.g., Cassisi & Salaris 2013, and references therein). This is true for the interiors of brown dwarfs (see, e.g., Chabrier & Baraffe 2000, for a review), the helium cores of low-mass stars (masses below ∼2.0–2.3 $M_{\odot}$) during their red giant branch (RGB) evolution (see, e.g., Salaris et al. 2002, for a review of RGB models), the carbon-oxygen cores of low- and intermediate mass stars (masses below 6–7 $M_{\odot}$) during the asymptotic giant branch (AGB) phase (see, e.g., Cassisi & Castellani 1993), the oxygen-neon cores of super-AGB stars with masses between ∼6–7 and ∼10 $M_{\odot}$ (see, e.g., Garcia-Berro & Iben 1994; Siess 2007), the cores and parts of the H-He envelopes of white dwarfs (WDs – see, e.g., Fontaine et al. 2001), as well as the envelopes of neutron stars (see, e.g., Beznogov et al. 2021, for a review).

The calculation of the electron conduction opacity in astrophysical plasmas is an ongoing enterprise, with a decades-long history, starting with the works by Marshak (1941), Lee (1950), Mestel (1950), elaborated upon in the seminal works by Spitzer & Härm (1953), Chapman (1954), Braginskii (1958), and the widely employed calculations by Hubbard & Lampe (1969) further developed by Itoh and co-authors (Flowers & Itoh 1976, 1979, 1981; Itoh et al. 1984; Mitake et al. 1984; Itoh & Kohyama 1993), and Yakovlev and co-authors (Yakovlev & Urpin 1980; Urpin & Yakovlev 1980; Raikh & Yakovlev 1982; Yakovlev 1987; Baiko & Yakovlev 1995; Baiko et al. 1998), which were summarized, refined, and employed in extensive calculations by Potekhin et al. (1999, hereafter P99).

Each of these sources of opacities carried its own limitations and shortcomings. For instance, Spitzer & Härm (1953) considered non-degenerate electrons, while Hubbard & Lampe (1969) used different methods of calculations in cases of weak and strong electron degeneracy, for instance, when $T \gg T_{\rm F}$ and $T \ll T_{\rm F}$, where T is the temperature and $T_{\rm F}$ is the Fermi temperature (see Sect. 2.1), leaving some gaps in the intermediate range of partially degenerate electrons, where $T \sim T_{\rm F}$. In addition, Hubbard & Lampe tabulations covered a very limited set of chemical mixtures, and neither Spitzer & Härm nor Hubbard

& Lampe took into account the relativistic effects or the regime of dense matter where the stellar plasma solidifies. The work by Itoh's and Yakovlev's research groups made significant improvements over the previous results, taking into account the effects of special relativity and more accurate structure factors for the electron-ion plasmas, as well as the electron-phonon scattering that replaces the electron-ion scattering in the solid phase. Their results could be employed also to compute opacities for arbitrary chemical mixtures, however they covered only the case of strong electron degeneracy, namely, a regime where $T \ll T_{\rm F}$, which is not really fulfilled in the He-cores of RGB stars or the envelopes of WDs (see e.g., Catelan 2007, and the next sections for a deeper analysis of this issue).

For the conductive opacities due to the electron-ion (ei) scattering, a consistent way of filling the gap between the domains of weakly and strongly degenerate electrons is provided by the thermal averaging procedure (see e.g., Cassisi et al. 2007, hereafter C07), patterned after the method previously employed by Potekhin & Yakovlev (1996) to compute finite-temperature effects on the Shubnikov–De Haas oscillations of the electron transport coefficients of degenerate electron-ion plasmas in quantizing magnetic fields[1]. Unfortunately, this method is not applicable to the electron-electron (ee) scattering: to overcome this difficulty, an interpolation formula has been proposed by C07, who have also taken into account an improved treatment of the ee scattering at high densities, which was suggested at the time by Shternin & Yakovlev (2006).

The electron conduction theory has undergone substantial progress in the last decade, enabling further refined studies of the heat transport by partially degenerate electrons (e.g., Desjarlais et al. 2017; Daligault 2018; Shaffer & Starrett 2020, and references therein). In particular, Shaffer & Starrett (2020) demonstrated that the ee scattering affects the thermal conductivity in a non-trivial way at $T \sim T_{\rm F}$, resulting in lower conductive opacities compared to the traditional approach. This effect is especially pronounced for light chemical elements in the regime of moderate coupling and moderate degeneracy. Based on this theory, Blouin et al. (2020, hereafter B20) calculated the conductive opacities for H and He compositions, finding a difference by up to a factor 2.5–3 as compared to C07 near the boundary of the temperature-density domain, where the new theory may be applied. They have also shown that this decrease of the conductive opacities has a sizable impact on the cooling times of WD models with H and He envelopes, such that the age of the coolest models is reduced by as much as ∼2 Gyr, as compared to calculations with C07 opacities.

The important point to notice is, as also stated by Shaffer & Starrett (2020) and B20, that the traditional (e.g., C07) results are superior at a strong degeneracy because unlike B20, these ensure the known asymptotic limits at $T/T_{\rm F} \ll 1$. In addition, the theory underlying the B20 results is non-relativistic and, therefore, it is restricted to mass densities $\rho \lesssim 10^6\,{\rm g\,cm^{-3}}$. Therefore, we need to bridge B20 results for mildly degenerate, non-relativistic plasmas and the traditional opacities at higher densities. This introduces some uncertainty, which can affect the calculation of both WD and RGB models, for sizable portions of the helium cores of RGB models and of the H and He envelopes of WD models, covering a range of the degeneracy parameter $\theta \equiv T/T_{\rm F}$ that extends from a few times 0.01 to a few times 0.10 and above.

The purpose of this paper is to investigate different possible ways to merge B20 results at $\theta \sim 1$ with the opacities at $\theta \ll 1$, studying their impact on the cooling times of WD models and on the mass of the electron degenerate helium cores of low-mass stellar models at the He-flash, as well as the resulting effect on the RGB lifetime, the luminosities of the tip of the RGB, and the start of quiescent core He-burning after the degeneracy has been lifted. These luminosities are traditionally used to constrain the distance of old stellar populations (ages above 1–2 Gyr).

The plan of the paper is as follows. In Sect. 2, we summarise the theoretical background to the calculations of conductive opacities, give an overview of the recent updates for the partially degenerate domain, and discuss possible ways to treat the transition to the strong degeneracy regime. Section 3 presents our stellar evolution calculations and discusses the impact of the new conductive opacities and the related uncertainties on the results. Our summary and conclusions follow in Sect. 4.

2. Conductive opacities

In stationary and non-convective layers of a star, the heat transport is governed by the Fourier law $\boldsymbol{F} = -\lambda\,\nabla T$, where $\boldsymbol{F}$ is the heat flux, T is the temperature, and λ the thermal conductivity. The last quantity is related to the opacity κ by the equation (see e.g., Kippenhahn et al. 2012)

$$\kappa = \frac{16\sigma T^3}{3\rho\lambda}, \tag{1}$$

where σ is the Stefan-Boltzmann constant and ρ is the mass density.

In general, radiative and conductive energy transports work in parallel; hence, the total thermal conductivity is the sum $\lambda = \lambda_{\rm r} + \lambda_{\rm e}$, where $\lambda_{\rm r}$ and $\lambda_{\rm e}$ denote the radiative (r) and electron (e) components of the thermal conductivity λ. Accordingly, $\kappa^{-1} = \kappa_{\rm r}^{-1} + \kappa_{\rm c}^{-1}$, where the radiative (r) and conductive (c) opacities are related, respectively, to $\lambda_{\rm r}$ and $\lambda_{\rm e}$ by Eq. (1).

The transport coefficients of the electron-ion plasmas in the case of non-degenerate and non-relativistic electrons ($T \gg T_{\rm F}$, $x_{\rm r} \ll 1$), and weakly coupled ions ($\Gamma_{\rm i} \ll 1$, where $\Gamma_{\rm i} = (4\pi n_{\rm ion}/3)^{1/3}(Ze)^2/k_{\rm B}T \approx (2.275\times10^7{\rm K}/T)\,Z^{5/3}x_{\rm r}$ is the Coulomb coupling parameter) were calculated long ago (e.g., Spitzer & Härm 1953; Chapman 1954; Braginskii 1958) using the classical theory by Chapman & Cowling (1970). The theory of the thermal conduction by electrons of arbitrary degeneracy in the fully ionized non-relativistic stellar interior was reviewed by Hubbard & Lampe (1969). An extension to the degenerate electron gas with allowance for the special relativity effects was described in detail by Flowers & Itoh (1976).

2.1. Theoretical background

When dealing with electron conduction, according to the elementary theory based on the kinetic method and on the assumption that the effective electron scattering rate ν does not depend on the electron energy, $\lambda_{\rm e}$ can be written as (Ziman 1960):

$$\lambda_{\rm e} = \frac{3}{2}\,\frac{n_{\rm e}k_{\rm B}^2T}{m_{\rm e}^*\nu} \ \text{ at } T \gg T_{\rm F}, \quad \lambda_{\rm e} = \frac{\pi^2}{3}\,\frac{n_{\rm e}k_{\rm B}^2T}{m_{\rm e}^*\nu} \ \text{ at } T \ll T_{\rm F}, \tag{2}$$

where $n_{\rm e}$ is the electron number density, $m_{\rm e}^*$ is the effective dynamical electron mass, $k_{\rm B}$ is the Boltzmann constant, c is

[1] We note that here we consider non-magnetized plasmas and focus on their thermal conductivity in the liquid phase. For a more general overview of the recent progress in the theory of conductivities in the Coulomb plasmas, including the solid phase and the magnetized plasmas, see e.g., Potekhin et al. (2015) and references therein.

the speed of light, and T_F is the electron Fermi temperature. At $T \ll m_e c^2/k_B = 5.93\times10^9$ K, the effective electron mass is given by $m_e^* = m_e\sqrt{1+x_r^2}$, where m_e is the true electron mass, and x_r is the relativity parameter:

$$x_r \equiv \frac{p_F}{m_e c} \approx \left(\rho_6 \frac{Z}{A}\right)^{1/3}. \quad (3)$$

Here, $\rho_6 \equiv \rho/10^6\,\mathrm{g\,cm^{-3}}$, $p_F = \hbar(3\pi^2 n_e)^{1/3}$ is the Fermi momentum, Z and A are, respectively, the ion charge and mass numbers. In mixtures of elements with different charge numbers Z_j, they should be averaged using the number fractions $x_j = n_j/n_{ion}$ of the components as weights, viz. $\langle Z\rangle \equiv \sum_j x_j Z_j$ (where n_j is the number of ions of species j and $n_{ion} = n_e\langle Z\rangle^{-1}$ the total number of ions, per unit volume); the same holds for A_j. The Fermi temperature:

$$T_F = \frac{m_e c^2}{k_B}\left(\sqrt{1+x_r^2}-1\right) \quad (4)$$

determines whether the electrons are non-degenerate ($T_F \ll T$), strongly degenerate ($T_F \gg T$), or mildly degenerate ($T_F \sim T$). In the non-relativistic theory, which is valid at $x_r \ll 1$, we have $m_e^* = m_e$ and $T_F \approx 3\times10^9\,(\rho_6\,Z/A)^{2/3}$ K.

Beyond the elementary transport theory, it is still convenient to use Eq. (2), but in this case ν is some 'effective' collision frequency. In the fully ionized gas or liquid, the electron heat conduction is limited by the ei and ee scattering; the assumption that the scattering rates of different kinds are mutually independent results in the so called Matthiessen's rule, positing that the collision frequencies simply add up. Then, in the fully ionized liquid or gas,

$$\nu = \nu_{ei} + \nu_{ee}, \quad (5)$$

where ν_{ei} and ν_{ee} are the frequencies of the electron scattering on the ions and on the electrons, respectively.

The ei collision frequency in a strongly degenerate Coulomb liquid can be written in the form (e.g., Yakovlev & Urpin 1980):

$$\nu_{ei} = 4\pi Z^2 e^4 n_{ion}\, m_e^*\, p_F^{-3}\Lambda(p_F), \quad (6)$$

where $\Lambda(p_F)$ is a dimensionless Coulomb logarithm. It is possible to compute conductivities determined by elastic ei scattering at arbitrary degeneracy, using a specific thermal averaging, which involves an energy-dependent effective collision frequency, described by Eq. (6) at every isoenergetic surface, corresponding to a given p_F (e.g., C07; Potekhin & Yakovlev 1996; Ventura & Potekhin 2001).

Although the ei scattering is usually most important for degenerate plasmas, the ee scattering is non-negligible for $Z \lesssim 10$, which is especially important for H and He. Lampe (1968a) treated the ee scattering using the Chapman-Enskog solution of the quantum Lenard-Balescu kinetic equation for the system of degenerate electrons and point-like, non-degenerate, weakly coupled classical ions. The dynamical screening of the electrons was treated in the random-phase approximation, applicable at $T \ll T_F$. The author showed that the character of the scattering is different at temperatures $T \ll T_{pl}$ and $T_{pl} \ll T \ll T_F$, where

$$T_{pl} = \frac{\hbar}{k_B}\left(\frac{4\pi n_e e^2}{m_e^*}\right)^{1/2} \quad (7)$$

is the electron plasma temperature. In a subsequent paper, Lampe (1968b) applied the Chapman-Enskog solution of the quantum Lenard-Balescu kinetic equation to the non-degenerate and weakly degenerate electrons.

Hubbard & Lampe (1969) combined these calculations with the earlier results of Hubbard (1966), who considered the ei opacities, κ_{ei}, in a non-relativistic degenerate electron gas, taking into account the ion-ion correlations. Hubbard and Lampe provided conductive opacities in tabular form for various chemical compositions. Due to the use of different approximations for non-degenerate and degenerate electrons, their tables for these two cases do not match each other smoothly and thus contain gaps at sufficiently low temperatures (see more details in C07).

Hubbard and Lampe used the non-relativistic theory. The expression of ν_{ee} for the relativistic degenerate electrons was obtained by Flowers & Itoh (1976) at $T \ll T_{pl}$, and extended by Urpin & Yakovlev (1980) to higher temperatures, where $T_{pl} \lesssim T \ll T_F$. Shternin & Yakovlev (2006) reconsidered the problem including the Landau damping of transverse plasmons, neglected by the previous authors. They showed that the Landau damping strongly increases ν_{ee} in the domain of $x_r \gtrsim 1$, $\theta \ll 1$, and $T \ll T_{pl}$. Their fit to to ν_{ee} is widely used in studies of degenerate stars and, in particular, it was employed by C07.

2.2. Suppression of opacities in partially degenerate plasmas

Matthiessen's rule (see Eq. (5)) results in the additivity of the ei and ee opacities:

$$\kappa_c = \kappa_{ei} + \kappa_{ee}, \quad (8)$$

and can be derived in the lowest (one-polynomial) approximation of the Chapman-Enskog method (Chapman 1954; Hubbard & Lampe 1969). However, as stated by Hubbard & Lampe (1969), at least the two-polynomial approximation should be used to obtain accurate results, the accuracy provided by the Matthiessen's rule was deemed to be sufficient for astrophysical applications because using the variational principle of the kinetic theory, it can be shown that $\nu_{ei}+\nu_{ee} \le \nu \le \nu_{ei}+\nu_{ee}+\delta\nu$, where $\delta\nu \ll \min(\nu_{ei},\nu_{ee})$ (see e.g., chapter 7 of Ziman 1960). However, this relation implies that the shape of the electron distribution function is the same with and without the ee collisions. In fact, the electron distribution function takes on a different shape depending on whether or not the ee collisions occur.

Desjarlais et al. (2017) posited a modified Matthiessen's rule in the form:

$$\kappa_c = S_\kappa \kappa_{ei} + \kappa_{ee}, \quad (9)$$

where S_κ is a 'reshaping correction', representing the indirect modification of the ei scattering term due to the ee interaction. Desjarlais et al. (2017) computed hydrogen electrical and thermal conductivities by the QMD method using the Kohn-Sham density-functional theory together with a Kubo-Greenwood response framework and compared the results with the quantum Lenard-Balescu solution in the regime of weak ion coupling ($\Gamma_i \ll 1$) and moderate degeneracy ($T \sim T_F$), where both methods are applicable. They found that the reshaping factor can be as low as $S_\kappa \sim 0.6$.

Daligault (2016, 2017, 2018) extended the formulas for the transport coefficients of classical plasmas inside the dense plasma regime by applying the Chapman-Enskog method to solve the quantum Landau-Fokker-Planck (qLFP) kinetic equation. The qLFP equation extends the classical LFP equation by accounting for the Pauli principle while retaining the small-angle collision approximation. This extension has become possible due to modifications to the classical Chapman-Enskog

method. In particular, Daligault (2018) replaced the expansion over the classical Sonine polynomials by a set of orthogonal 'quantum' polynomials. Moreover, he derived practical formulas for the calculation of transport coefficients (electrical and thermal conductivities, viscosity, diffusion coefficients) based on this new polynomial expansion. He has demonstrated that with his method we can extend the range of validity of the classical LFP equation, determined by the strong inequality $T \gg T_{\rm F}$, to lower temperatures. For example (see Fig. 1 in Daligault 2018, where $r_s = 0.014/x_{\rm r}$), the 10% accuracy is ensured by the classical LFP approximation at $T > 4T_{\rm F}$, while the qLFP approximation provides the same accuracy at $T > 1.7T_{\rm F}$ and $x_{\rm r} > 0.005$, at $T > T_{\rm F}$ and $x_{\rm r} > 0.16$, and also at $T > 0.3T_{\rm F}$ and $x_{\rm r} > 0.25$.

In both LFP and qLFP cases the plasma was assumed to be weakly coupled and non-relativistic, and these approximations impose supplementary restrictions on the validity domain, which can be roughly put as $\Gamma_{\rm i} \ll 1$ and $x_{\rm r} \lesssim 1$. In addition, the effects of electron exchange are neglected. The exchange effects always reduce the electron scattering rate, but no more than by a factor of two (see Daligault 2017).

Very recently, Shaffer & Starrett (2020) have combined the qLFP theory with the concept of mean-force scattering, where the scattering cross-sections are calculated using the potential of mean force as the interaction potential. This way they can account for strong coupling effects in a plasma kinetic framework and alleviate the constraint $\Gamma_{\rm i} \ll 1$. They found a significant suppression of the effective ee scattering rate in a finite temperature interval, caused by non-monotonicities in the ee mean-force potential as an indirect effect of strong ion coupling. The inclusion or omission of ee collisions in qLFP is rather unimportant for the electrical conductivity at low temperatures, whereas the thermal conductivity still depends on ee collisions at any temperature. In the limit of a fully degenerate electron gas, $T/T_{\rm F} \to 0$, the thermal conductivity obtained with this method is identical to that of an electron gas, which is clearly unrealistic. Shaffer & Starrett (2020) concluded that this unphysical behavior at low temperatures is an artifact of the small-angle approximation and these authors traced a connection to the argument by Lampe (1968a), who noted that large-angle ee collisions are more strongly Pauli blocked than ei ones, whereas small-angle collisions are less so. Therefore, the qLFP method, while successful over a wide range of temperatures, still breaks down for sufficiently degenerate plasmas, in agreement with the above-mentioned considerations by Daligault (2017, 2018). In addition, the method may fail in the case of very strongly coupled Coulomb plasmas, where an accurate ion structure factor is needed to grasp the long-range order effects (Baiko et al. 1998; Wetta & Pain 2020).

2.3. Bridging the opacities of mildly and strongly degenerate H and He plasmas

B20 applied the method of Shaffer & Starrett (2020) to the calculation of conductive opacities for pure H and He compositions. In case of heavier elements, the electron-electron interactions are less important, so that this method is expected to produce results more similar to the conductive opacities $\kappa_{\rm c}$ obtained using the Matthiessen's rule, that is, by assuming $S_\kappa = 1$. Hereafter, following B20, we denote the latter opacities as $\kappa_{\rm c}^{\rm Ioffe}$. They are essentially the C07 opacities but improved as described in Potekhin et al. (2015); the differences with the original C07 opacities for liquid H and He plasmas are at most within 2%.

B20 found a substantial reduction of the conductive opacities (corresponding to an enhancement of the thermal conductivity) in the domain of partial degeneracy, compared to $\kappa_{\rm c}^{\rm Ioffe}$. Their Tables 1 and 2 provide $\kappa_{\rm c}$ for pure H and pure He compositions, which at fixed temperature, T, reach densities corresponding to $\theta \equiv T/T_{\rm F}$ generally between 0.2 and 0.1. The difference with $\kappa_{\rm c}^{\rm Ioffe}$ exceeds a factor of 2 on the verge of this density-temperature domain.

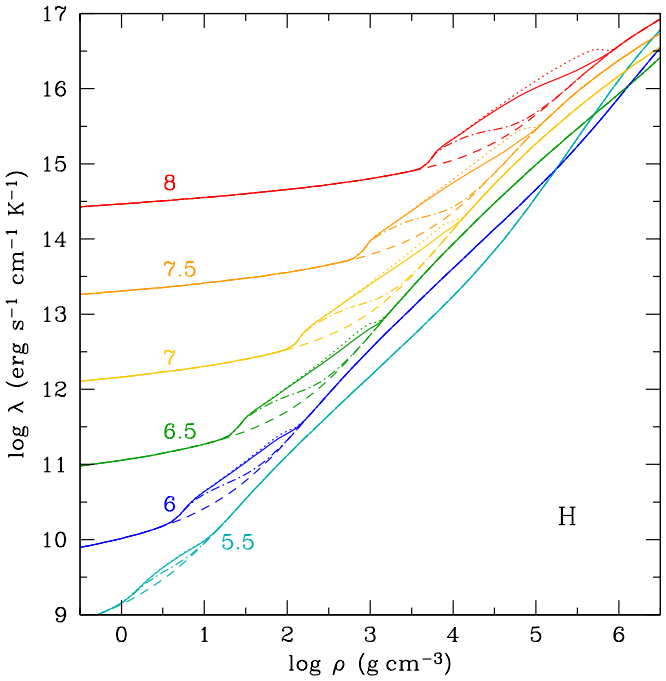

Fig. 1. Thermal conductivity for hydrogen as function of mass density for several constant temperatures T. Dashed lines show the traditional conductivities $\lambda_{\rm e}^{\rm Ioffe}$, and dotted lines display the conductivities $\lambda_{\rm e}^{\rm B20} = F\lambda_{\rm e}^{\rm Ioffe}$ enhanced by the F factor in Eq. (11). The solid and dot-dashed lines show the conductivities with the weakly and strongly damped corrections given by Eq. (12), $\lambda_{\rm e}^{\rm B20wd}$ and $\lambda_{\rm e}^{\rm B20sd}$, respectively. They provide two different transitions from the new calculations for partially degenerate electrons $\lambda_{\rm e}^{\rm B20}$ to the traditional results $\lambda_{\rm e}^{\rm Ioffe}$ in the strong degeneracy regime (see details in the text). Numbers near the curves mark log T(K) values.

To facilitate the implementation of their new opacity calculations in stellar evolution codes, B20 devised an analytic expression for the factor (denoted hereafter by F) to reduce the the traditional opacity to fit their numerical results. Accordingly, the reduced conductive opacity and enhanced thermal electron conductivity is given as:

$$\kappa_{\rm c} = \kappa_{\rm c}^{\rm Ioffe}/F, \quad \lambda_{\rm e} = F\lambda_{\rm e}^{\rm Ioffe}. \tag{10}$$

The correction factor is written as:

$$F = 1 + g(x,y)H(g(x,y)), \tag{11}$$

where $x = \log(\rho/\rho_0)$, $y = \log(T/T_0)$, $\rho_0 = 10^{5.45}\,{\rm g\,cm^{-3}}$ and $T_0 = 10^{8.40}\,{\rm K}$ for hydrogen, $\rho_0 = 10^{6.50}\,{\rm g\,cm^{-3}}$ and $T_0 = 10^{8.57}\,{\rm K}$ for helium, function $g(x,y)$ is a tilted scaled Gaussian, and $H(g)$ is a correction to the Gaussian shape at large g (see the explicit formulas given in B20). This fit accurately reproduces the numerical B20 results at $\theta > 0.1$ and ensures that the correction vanishes when $\theta \to 0$. Hereafter $\kappa_{\rm c}^{\rm B20}$ and $\lambda_{\rm e}^{\rm B20}$ denote, respectively, the opacities and thermal conductivities given by Eqs. (10) and (11).

The electron thermal conductivities calculated with and without the correction factor by B20 are shown in Fig. 1 for

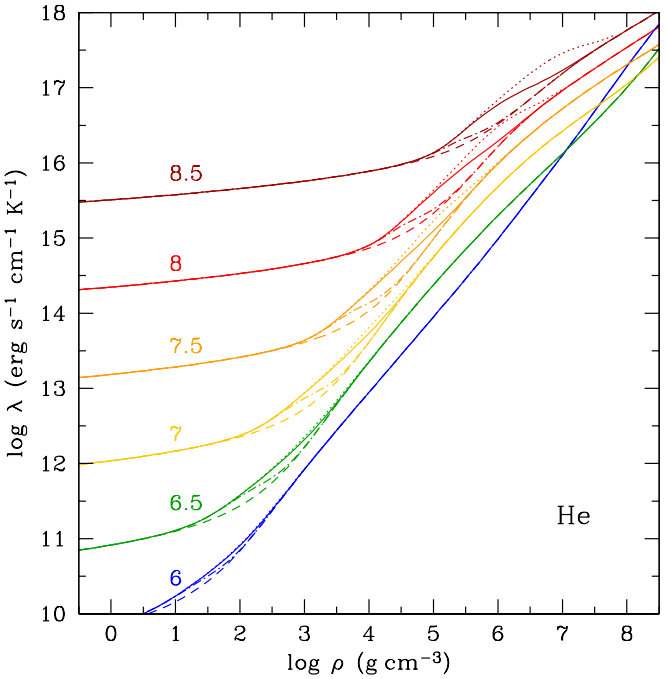

Fig. 2. Thermal conductivity for helium as a function of mass density for several constant temperatures T. The meaning of the various lines is the same as in Fig. 1.

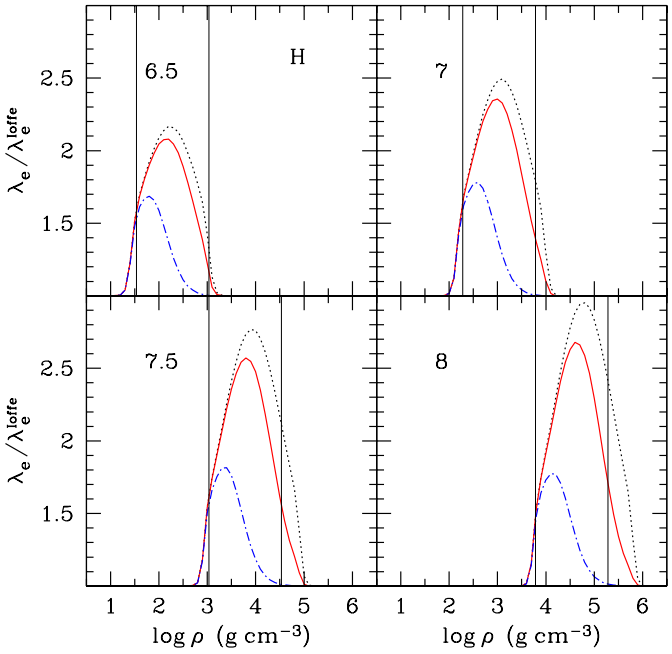

Fig. 3. Ratio of the electron thermal conductivity for hydrogen enhanced according to B20 (λ_e^{B20}) to λ_e^{Ioffe} results, as a function of $\log\rho$ (dotted lines), for the labelled values of $\log T$, with T given in Kelvin. Solid lines display the analogous ratio for the thermal conductivities λ_e^{B20wd} obtained using the weakly damped enhancement factor F. Dot-dashed lines show the corresponding ratio for the strong damping, λ_e^{B20sd}. The vertical lines mark the boundaries of the range of densities corresponding to $\theta = 1$ and $\theta = 0.1$ (higher ρ implies lower θ, at constant T).

hydrogen, and in Fig. 2 for helium, in the relevant T and ρ ranges. The convergence of λ_e^{B20} to the traditional estimate λ_e^{Ioffe} is rather slow at high densities, if the temperature is also high. In this case the B20 correction does not vanish until $T \ll 0.1T_F$, which is certainly far beyond the range of validity of Shaffer & Starrett (2020) method and most likely overestimates the true enhancement of the conductivities in these cases.

This is shown even more clearly in Figs. 3 and 4, which display the ratio $\lambda_e^{B20}/\lambda_e^{Ioffe}$ as a function of ρ for several temperatures T; densities corresponding to $\theta = 0.1$ and 1.0 are also marked. For example, at $T > 10^7$ K convergence is reached only at densities corresponding to T_F values well above $10\,T$, that is, at $\theta \ll 0.1$. In addition, broad differences between the dashed and dotted lines are observed in the case of helium at $\rho > 10^6$ g cm^{-3}, where the electrons are relativistic.

To achieve a faster convergence to the degenerate asymptote in the regime of strong degeneracy, we introduced a damping factor $D(\theta) = (1+a\theta^{-b})^{-1}$ ($\theta \equiv T/T_F$). The damped enhancement factor F for the electron thermal conductivity (a reduction factor for the conductive opacities) then reads

$$F = 1 + \frac{g(x,y)H(g(x,y))}{1 + a\,(T_F/T)^b}. \quad (12)$$

Given that the qLFP equation is non-relativistic, we use the non-relativistic approximation for T_F in Eq. (12). We have made two choices of the parameters a and b. A conservative choice (that we denote as 'weak damping') is to ensure that $D(\theta)$ does not change F by more than 1% at $T > T_F$ and that it does not exceed 1% (ensuring that $F \approx 1$) at $T < 0.01T_F$. These conditions are fulfilled for $a = 0.01$ and $b = 2$. The electron conductivities obtained using this weakly damped enhancement factor, which we denote by λ_e^{B20wd} are shown in Figs. 1 and 2 (the corresponding opacities will be denoted by κ_c^{B20wd}), while the ratio of λ_e^{B20wd} to λ_e^{Ioffe} as a function of ρ is shown in Figs. 3 and 4.

We can see that λ_e^{B20} and λ_e^{B20wd} almost coincide at $T > T_F$ (to the left of the left vertical line in Figs. 3 and 4), ensuring that our damping does not distort the B20 results in the domain where the underlying approximations are reliable. The weak damping is seen to provide a good agreement with B20 results for T down to $0.5\,T_F$, while at the same time it almost fully converges to the traditional results at $T \lesssim 0.03\,T_F$. The ratio $\lambda_e^{B20wd}/\lambda_e^{Ioffe}$ is however sometimes still quite substantial (up to a factor of ~1.5) at $T \sim 0.1T_F$, where λ_e^{Ioffe} may be already preferable, as discussed also by B20. Indeed, as we see in Sect. 2.2, the results and discussions from Daligault (2017, 2018) and Shaffer & Starrett (2020) prompt the assumption that these approximations, which are inherent to the qLFP method (in particular, the small-angle scattering approximation) may lead to an uncertainty of ~10% at $T = T_F$ and to implausible results at $T \ll T_F$.

We cannot therefore exclude that in reality the conductivity should converge to λ_e^{Ioffe} more rapidly in the transitional range $0.1T_F \lesssim T \lesssim T_F$. To this end, we considered a much more extreme, but probably still realistic 'strong damping' choice, defined by the requirements that $D(\theta)$ does not affect F by more than 10% at $T > T_F$ and that $D(\theta)$ does not exceed 1% at $T < 0.1T_F$. In this case, $a = 0.1$ and $b = 3$ in Eq. (12). The conductivities (see Figs. 1 and 2) and opacities obtained with such strongly damped enhancement factor will be denoted by λ_e^{B20sd} and κ_c^{B20sd}, respectively.

The ratio of λ_e^{B20sd} to λ_e^{Ioffe} as a function of ρ is also displayed in Figs. 3 and 4, which show how λ_e^{B20sd} converges to λ_e^{Ioffe} at $T \sim 0.1\,T_F$, whilst it is almost equal to λ_e^{B20} at $T > T_F$. The values of λ_e^{B20sd} may noticeably (up to ~30%) differ from the B20 calculations already at $T \sim 0.5\,T_F$; however, we believe that this strong damping option is a plausible extreme choice. As we

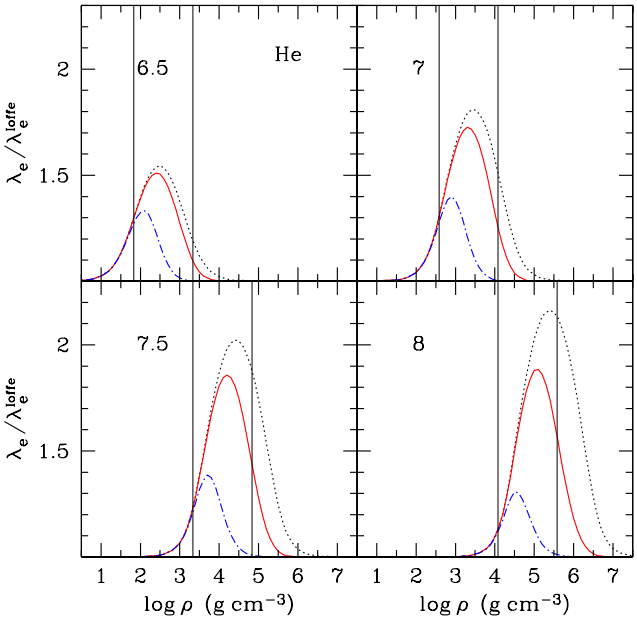

Fig. 4. Ratio of the electron thermal conductivity for helium enhanced according to B20 to λ_e^{Ioffe}, as a function of logρ, for the labelled values of log(T). The meaning of the various lines is the same as in Fig. 3.

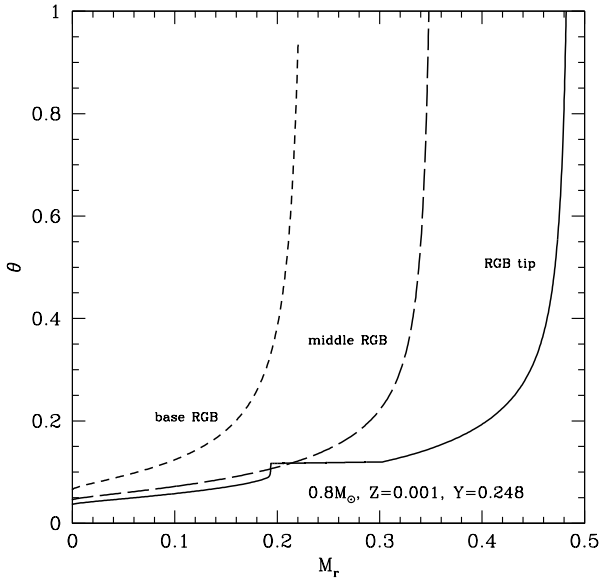

Fig. 5. Run of the ratio $\theta \equiv T/T_F$ as a function of the mass (in solar units) enclosed within a distance r from the centre, for the He-core at three different stages of the RGB evolution of a model with the labelled total mass, initial helium mass fraction Y and a metal mass fraction Z (metal distribution α-enhanced, with [α/Fe] = 0.4, typical of Galactic halo stars) corresponding to [Fe/H] = −1.5. The discontinuity at $M_r \approx 0.2\,M_\odot$ in the structure corresponding to the TRGB stellar model is due to off-center He-burning ignition that starts removing the electron degeneracy.

have discussed in Sect. 2.2, the inaccuracy of the qLFP method may reach 10% at $T \sim T_F$, hence, it is not unrealistic to assume still greater inaccuracies at $T \sim 0.5\,T_F$.

The differences between these three choices of the electron conductivity (B20, B20 with weak damping, and B20 with strong damping) are, by construction, maximal around $\theta \sim 0.1$ (within a factor of 3), which is a θ range encountered in RGB He-cores and WD envelopes, as shown in Figs. 5 and 6.

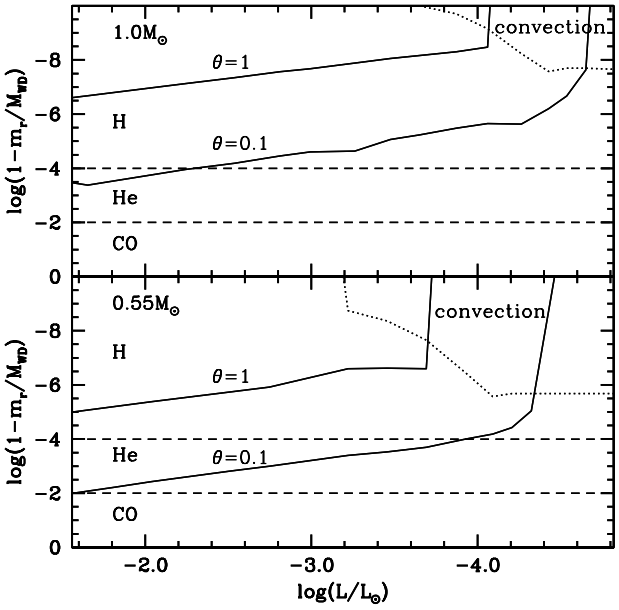

Fig. 6. Evolution with the surface luminosity L of selected physical and chemical quantities across WD models with masses equal to 0.55 and 1 $M_\odot$. The vertical axis displays the logarithm of the mass m_r enclosed between the surface and a point at a distance r from the centre, normalised to the total WD mass M_{WD}. Dashed lines mark the boundaries of the carbon-oxygen core as well as the helium and the hydrogen envelope. The lower boundary of surface convection is denoted by dotted lines. The solid lines show the position of the mass layers where $\theta = 1$ and 0.1.

Figure 5 displays the run of θ across the structure of the He-core at three selected luminosities during the RGB evolution of a typical low-mass (0.8 $M_\odot$), metal poor stellar model (from Pietrinferni et al. 2021). In all three cases, T/T_F ranges between ∼0.05 at the centre of the He-core and ∼1 at its outer edge.

A sketch of the internal structures of two WD models (for DA WDs with He and H envelopes, from Salaris et al. 2010) and their evolution with the surface luminosity is shown in Fig. 6, for masses equal to 0.55 and 1 $M_\odot$, bracketing the typical mass range of carbon-oxygen WDs. For both masses, the layers where T/T_F is around 0.1 are located in the He or the H layers, depending on the model luminosity. The same is true in models with just He envelopes (for DB WDs).

3. Effects on stellar models

In this section, we quantify the effect of using alternatively κ_c^{Ioffe} (C07), κ_c^{B20} (B20), κ_c^{B20sd} (B20sd), and κ_c^{B20wd} (B20wd) opacities on RGB (and the following horizontal branch stage) and WD models. For the RGB computations, we relied on the same stellar evolution code, physical assumptions (including atomic diffusion), and input physics adopted by Pietrinferni et al. (2021). The calculations by Pietrinferni et al. (2021) make use of C07 conductive opacities, hence, they are taken as a reference in the following discussion. For the WD models, we employed the code and physics inputs described by Salaris et al. (2010).

3.1. Red giant branch and horizontal branch models

We computed models for initial masses in the range 0.8–2.4 $M_\odot$ and various chemical compositions, from the pre-main sequence stage until the He-burning ignition at the tip of the RGB (TRGB),

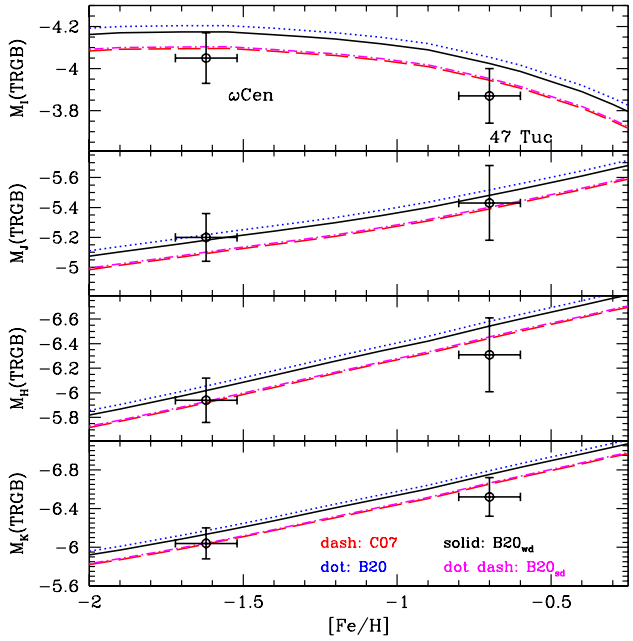

Fig. 7. Theoretical TRGB absolute magnitudes in the I (Cousins) and JHK (Bessel & Brett system) filters as a function of [Fe/H], for the four choices of conductive opacities discussed in this section (see labels and text for details). We also show (circles with error bars) the measured TRGB absolute magnitude in the Galactic globular clusters 47 Tuc and ω Centauri.

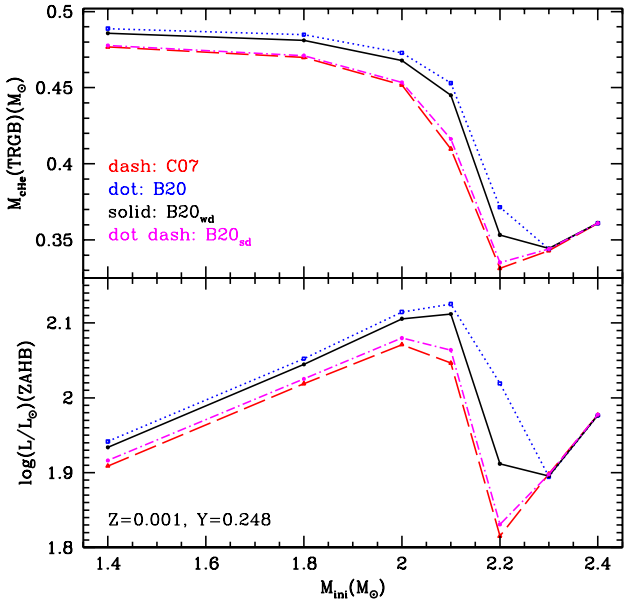

Fig. 8. The trend of selected structural and evolutionary properties for various assumptions about the conductive opacities. *Upper panel*: He-core mass at He-ignition as a function of the initial total mass for models with $Z = 0.001$ and $Y = 0.248$; *lower panel*: as the upper panel but for the bolometric luminosity at the beginning of the quiescent core He-burning, after the electron degeneracy has been lifted.

employing the same combinations of metallicity Z and initial helium abundance Y as in Pietrinferni et al. (2021).

We begin by analysing the results for the lower-end of the explored mass regime, that is, for the 0.8 $M_\odot$ models, which are characterised by a stronger electron degeneracy in their helium cores. The different choices of conductive opacities have a negligible impact on the RGB lifetime but, as expected, a sizable effect on the He-core mass at helium ignition ($M_{\rm cHe}$). Going from C07 to B20 opacities increases $M_{\rm cHe}$ by ∼0.01 $M_\odot$, independent of Z. If the opacities with weak damping B20wd are used instead, $M_{\rm cHe}$ increases by ∼0.007 $M_\odot$ compared to calculations with C07. Finally, the opacities with strong damping B20sd increase $M_{\rm cHe}$ by just ∼0.001 $M_\odot$.

Given that the TRGB brightness depends on the He-core mass at the He ignition, these differences translate to changes in the magnitude of the TRGB, an observable quantity, also used to determine distances to old stellar populations in galaxies. Figure 7 displays the $IJHK$ TRGB absolute magnitudes obtained from our calculations, for models with an age of 12–13 Gyr at the TRGB, and a large range of initial metallicities. Moving from C07 to B20 opacities makes the TRGB brighter by about 0.1 mag in all filters (because of the larger He-core masses), an increase which is reduced to about 0.07 mag when calculations with $\kappa_{\rm c}^{\rm B20wd}$ are considered instead. The use of $\kappa_{\rm c}^{\rm B20sd}$ instead of the C07 opacities has a negligible impact of the TRGB brightness of the models.

For the sake of comparison, we also show in Fig. 7 the absolute magnitudes of the TRGB determined for the Galactic globular clusters ω Centauri and 47 Tuc. We display Bellazzini et al. (2004) results, with small adjustments to take into account the recent distance determinations by Baumgardt & Vasiliev (2021).

The calculations using B20 and B20wd opacities predict TRGBs marginally brighter than the observed TRGB magnitudes in the I band – which, incidentally, have smaller measurement errors compared to the infrared data – when taking into account observational errors, while in JHK bands all sets of models are compatible with observations within the error bars. On balance these TRGB observations cannot definitely exclude any of the displayed four choices of conductive opacities. The marginal discrepancy with the more precise I-band data could for example be ascribed to some small (on the order of 0.01 mag) systematic errors in the calculations of the bolometric corrections, which might affect less severely the infrared bands.

We also investigated the impact of these different sets of opacities on RGB models with initial masses around the transition for the onset of electron degeneracy in the He-core. The upper panel of Fig. 8 shows $M_{\rm cHe}$ at the ignition of core He-burning for models with $Z = 0.001$ and $Y = 0.248$, and masses between 1.4 and 2.4 $M_\odot$. For masses larger than ∼1.4 $M_\odot$, the effect of choosing a different set of opacities increases, reaching a maximum between 2.1 and 2.2 $M_\odot$, to then vanish for larger masses, that do not develop electron degeneracy after the main sequence. For an initial mass of 2.1–2.2 $M_\odot$, the B20wd and B20 opacities increase $M_{\rm cHe}$ by ∼0.035 $M_\odot$ and ∼0.043 $M_\odot$, respectively. These differences still hold at other metallicities, the only change being systematic shifts of the values of the initial masses of the models around the transition, due to the effect of the initial metallicity (and He abundance) on the mass threshold for the onset of electron degeneracy.

These variations of the degenerate He-core masses at helium ignition affect the properties of the following core He-burning phase, as shown in both Figs 8 and 9. The lower panel of Fig. 8 shows the luminosity at the beginning of quiescent He burning, after the degeneracy has been lifted, for the models with initial masses between 1.4 and 2.4 $M_\odot$ and the labelled initial composition (we denote this stage by zero-age horizontal branch (ZAHB), as for the lower mass models, which are the theoretical counterpart of the stars that populate the horizontal branches of globular clusters) and the labelled initial

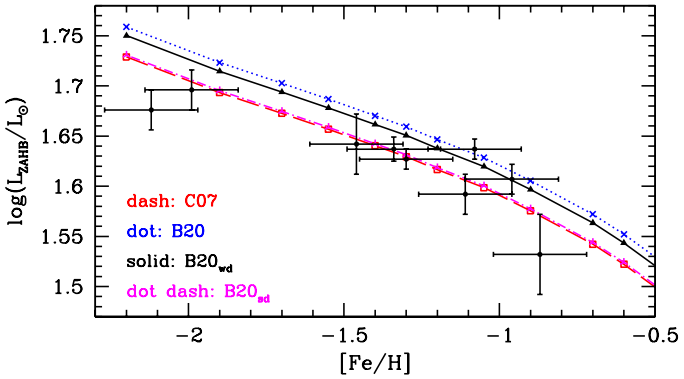

Fig. 9. Trend of the ZAHB brightness at the typical temperature of the RR Lyrae instability strip, as a function of [Fe/H] for the labelled choices of the conductive opacities. Points with error bars display semiempirical data for a sample of Galactic globular clusters (see text for details).

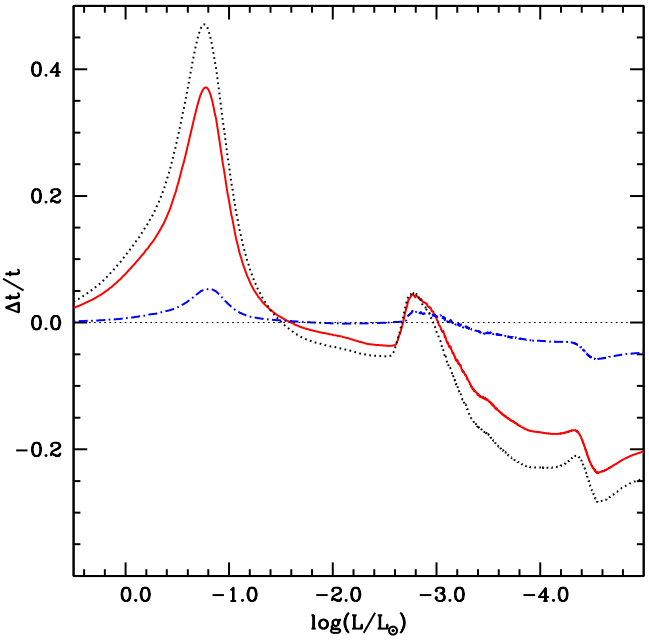

Fig. 10. Relative differences of the cooling times as a function of the surface luminosity, among different evolutionary models of a $1.0\,M_\odot$ DA WD. The dotted line displays the difference between calculations with C07 and B20 opacities (B20 cooling times minus C07 values at the same luminosity), the dot-dashed line the difference between B20sd and C07 calculations, and the solid line the difference between B20wd and C07 models.

composition. The variation of this luminosity with varying choices of the conductive opacities mirrors qualitatively that of $M_{\rm cHe}$, as expected. The effect is maximised for masses around $2.2\,M_\odot$, where $\Delta\log(L/L_\odot) \sim 0.2$ dex when passing from C07 to B20 opacities (the corresponding $\Delta\log(L/L_\odot)$ for the $1.4\,M_\odot$ models is equal to ∼0.03 dex) and ∼0.1 when B20wd opacities are used instead of C07.

The change in luminosity directly impacts on the core He-burning lifetime: For models with $1.4\,M_\odot$ the maximum effect amounts to a reduction on the order of 7% when B20 opacities are employed instead of C07, which increases to about 18% for models with mass around $2.2\,M_\odot$.

Figure 9 displays the theoretical ZAHB luminosity of lower mass models, at the typical temperature of the RR Lyrae instability strip ($\log T_{\rm eff} = 3.85$, with $T_{\rm eff}$ in K) as a function of the initial [Fe/H], obtained using alternatively the same four sets of conductive opacities. Again, the trends reflect the behaviour of $M_{\rm cHe}$ at He-ignition. Models calculated with the C07 opacities are the faintest ones, whilst those calculated with B20 opacities are about $\Delta\log(L/L_\odot) = 0.03$ more luminous. The calculations with the B20sd opacities are basically identical to the C07 ones, while the B20wd opacities provide ZAHB models $\Delta\log(L/L_\odot) \sim 0.02$ brighter than the C07 ones. The corresponding core He-burning lifetimes are affected at the level of at most 6–8% when adopting these different opacities.

The same figure also displays the semiempirical ZAHB luminosities for a sample of Galactic globular clusters, as determined by de Santis & Cassisi (1999), from the pulsational properties of their RR Lyrae stars. Due to the small sample size and the associated error bars, the comparison with the models does not set any definitive constraint on the appropriate way to bridge the regimes of moderate and strong degeneracy. Models based on C07 and the extreme case of the B20sd opacities, but also those based on B20 and B20wd opacities are to various degrees consistent with the data.

3.2. White dwarf models

B20 have already shown how WD cooling models are strongly affected by replacing $\kappa_{\rm c}^{\rm Ioffe}$ opacities in the calculations with the smaller $\kappa_{\rm c}^{\rm B20}$ values. Here, we make similar comparisons, but including also the cases of B20wd and B20sd opacities. We have considered a WD model with mass $M_{\rm WD} = 1.0\,M_\odot$, made of a carbon-oxygen core with chemical stratification taken from the solar progenitors' models by Salaris et al. (2010), surrounded by a helium envelope with mass equal to $10^{-2}M_{\rm WD}$, and a more external hydrogen envelope with mass equal to $10^{-4}M_{\rm WD}$. The code and input physics (except for the conductive opacities) are described in Salaris et al. (2010) and references therein. Such a high mass WD model is expected to display the strongest sensitivity to changes of the conductive opacities, as shown by B20.

Figure 10 shows the relative differences of the cooling times as a function of the surface luminosity, among our calculations with different opacity choices. Models calculated with B20 opacities have longer cooling times than C07 calculations – by up to about 40% – at luminosities above $\log(L/L_\odot) \sim -1.5$, where neutrino cooling is very efficient. As discussed by B20 (see also Salaris et al. 2013), the lower conductive opacities cause a faster cooling of the core, which reduces the efficiency of neutrino cooling and increases the cooling times at a given luminosity. In absolute terms, the cooling times in this phase are relatively short, on the order of at most 100 Myr when $\log(L/L_\odot) = -1.5$.

With decreasing luminosities, the cooling times with B20 opacities become increasingly shorter than C07 calculations, because of the faster cooling of the structure. This trend is temporarily broken in a narrow range of luminosities centred around $\log(L/L_\odot) \sim -2.6$, due to the earlier start of the crystallization in the models with B20 opacities, and the associated earlier onset of the release of latent heat and the extra energy due to carbon-oxygen phase separation (see e.g., Salaris et al. 2010, and references therein). At the typical luminosity of the faintest observed WDs ($\log(L/L_\odot) \sim -4.5$) the model calculated with B20 opacities has a cooling age of ∼9.5 Gyr, about 2.5 Gyr shorter than the corresponding calculations with C07 opacities. These differences are consistent with the results obtained by B20.

Calculations using the B20wd opacities display differences compared to C07 models, which are reduced by about 5-10%

compared to the previous case of using B20 opacities. As for RGB models and their core He-burning progeny, calculations with the B20sd opacities provide results almost identical to C07 models, with differences of the cooling times within ±5%.

4. Summary and conclusions

Electron conduction opacities are a key ingredient in the calculation of stellar models for low- and intermediate-mass stars, and a critical issue is centred on ways to bridge computations of conductive opacities in the regimes of moderate ($\theta \sim 1$) and strong ($\theta \lesssim 0.1$) degeneracy, which are necessarily calculated adopting different methods. In fact, the density-temperature regime at the transition between moderate and strong degeneracy is crucial for modelling the helium cores of RGB stars and the envelopes of WDs.

We discuss the case of bridging the new, improved conductive opacities calculated by B20 for the regime of moderate degeneracy and the calculations by C07 in the regime of strong degeneracy. We first considered B20 own analytical approximation, which, however, converges to C07 results only at $\theta \ll 0.1$, well into the regime of strong degeneracy. We then modified the B20 formula by introducing a physically motivated damping factor, which depends on the ratio $\theta = T/T_{\rm F}$, tuned in two alternative ways (weak and strong damping) to converge faster than the B20 fit to C07 results in the regime of strong degeneracy. Both damping prescriptions keep the B20 fit almost intact at $\theta > 1$. The weak damping option provides opacities still different from C07 at $\theta = 0.1$, whilst the more extreme strong damping converges to C07 opacities at $\theta = 0.1$, but it changes the B20 calculations already by 30% at $\theta \sim 0.5$, in the moderate degeneracy regime. As a consequence, these three sets of conductive opacities have large differences (up to a factor of ∼2) in the critical region around $\theta \sim 0.1$, which, in turn, have a major impact on the predicted RGB He-core masses (up to 0.01 $M_\odot$ for low-mass models far from the transition regime to non-degenerate He-cores, and up to ∼0.04 $M_\odot$ for masses around the transition), TRGB (up to ∼0.1 mag) and ZAHB luminosities (up to 0.03 dex for masses far from the transition, and up to ∼0.2 dex around the transition), and WD cooling times (up to 40–45% at high luminosities, and up to ∼25% at low luminosities).

Current observational constraints on the TRGB and ZAHB absolute magnitudes do not allow us to categorically exclude any of these options for the conductive opacities, also taking into account that there might be other sources of uncertainties on the theoretical predictions for these quantities. The much shorter cooling times predicted for faint, slowly evolving WDs by calculations with both the B20 fit and the weak damping option (compared to models calculated with opacities including the strong damping) will need to be tested against observations of WDs in old stellar populations.

We updated the table of non-magnetic electron conductivities available at the Ioffe Institute website[2] by implementing the correction factor in Eq. (12). We use the weak damping as our fiducial choice by default, but we consider also the strong damping as a realistic, albeit extreme possibility. We did not implement this correction directly in the computer code presented by the institute on their website, but we provided the corresponding subroutine and envisioned a possibility for its use (in the absence of a strong magnetic field) to correct the result of the main computation.

Acknowledgements. We thank our referees for constructive comments that have improved the presentation of our results. S. C. acknowledges support from Premiale INAF MITiC, from INFN (Iniziativa specifica TAsP), and from PLATO ASI-INAF agreement n.2015-019-R.1-2018. The work of AYP was supported by the Russian Science Foundation (grant 19-12-00133).

References

Baiko, D. A., & Yakovlev, D. G. 1995, Astron. Lett., 21, 702
Baiko, D. A., Kaminker, A. D., Potekhin, A. Y., & Yakovlev, D. G. 1998, Phys. Rev. Lett., 81, 5556
Baumgardt, H., & Vasiliev, E. 2021, MNRAS, 505, 5957
Bellazzini, M., Ferraro, F. R., Sollima, A., Pancino, E., & Origlia, L. 2004, A&A, 424, 199
Beznogov, M. V., Potekhin, A. Y., & Yakovlev, D. G. 2021, Phys. Rep., 919, 1
Blouin, S., Shaffer, N. R., Saumon, D., & Starrett, C. E. 2020, ApJ, 899, 46
Braginskii, S. I. 1958, Sov. Phys. - JETP, 6, 358
Cassisi, S., & Castellani, V. 1993, ApJS, 88, 509
Cassisi, S., & Salaris, M. 2013, Old Stellar Populations: How to Study the Fossil Record of Galaxy Formation (Wiley-VCH)
Cassisi, S., Potekhin, A. Y., Pietrinferni, A., Catelan, M., & Salaris, M. 2007, ApJ, 661, 1094
Catelan, M. 2007, in Graduate School in Astronomy: XI Special Courses at the National Observatory of Rio de Janeiro (XI CCE), eds. F. Roig, & D. Lopes, Am. Inst. Phys. Conf. Ser., 930, 39
Chabrier, G., & Baraffe, I. 2000, ARA&A, 38, 337
Chapman, S. 1954, ApJ, 120, 151
Chapman, S., & Cowling, T. G. 1970, The Mathematical Theory of Non-Uniform Gases, 3rd edn. (Cambridge: Cambridge University Press)
Daligault, J. 2016, Phys. Plasmas, 23, 032706
Daligault, J. 2017, Phys. Rev. Lett., 119, 045002
Daligault, J. 2018, Phys. Plasmas, 25, 082703
de Santis, R., & Cassisi, S. 1999, MNRAS, 308, 97
Desjarlais, M. P., Scullard, C. R., Benedict, L. X., Whitley, H. D., & Redmer, R. 2017, Phys. Rev. E, 95, 033203
Flowers, E., & Itoh, N. 1976, ApJ, 206, 218
Flowers, E., & Itoh, N. 1979, ApJ, 230, 847
Flowers, E., & Itoh, N. 1981, ApJ, 250, 750
Fontaine, G., Brassard, P., & Bergeron, P. 2001, PASP, 113, 409
Garcia-Berro, E., & Iben, I. 1994, ApJ, 434, 306
Hubbard, W. B. 1966, ApJ, 146, 858
Hubbard, W. B., & Lampe, M. 1969, ApJS, 18, 297
Itoh, N., & Kohyama, Y. 1993, ApJ, 404, 268
Itoh, N., Kohyama, Y., Matsumoto, N., & Seki, M. 1984, ApJ, 285, 758
Kippenhahn, R., Weigert, A., & Weiss, A. 2012, Stellar Structure and Evolution (Berlin-Heidelberg: Springer)
Lampe, M. 1968a, Phys. Rev., 170, 306
Lampe, M. 1968b, Phys. Rev., 174, 276
Lee, T. D. 1950, ApJ, 111, 625
Marshak, R. E. 1941, Ann. New York Acad. Sci., 41, 49
Mestel, L. 1950, Math. Proc. Cambridge Philos. Soc., 46, 331
Mitake, S., Ichimaru, S., & Itoh, N. 1984, ApJ, 277, 375
Pietrinferni, A., Hidalgo, S., Cassisi, S., et al. 2021, ApJ, 908, 102
Potekhin, A. Y., & Yakovlev, D. G. 1996, A&A, 314, 341
Potekhin, A. Y., Baiko, D. A., Haensel, P., & Yakovlev, D. G. 1999, A&A, 346, 345
Potekhin, A. Y., Pons, J. A., & Page, D. 2015, Space Sci. Rev., 191, 239
Raikh, M. E., & Yakovlev, D. G. 1982, Ap&SS, 87, 193
Salaris, M., Cassisi, S., & Weiss, A. 2002, PASP, 114, 375
Salaris, M., Cassisi, S., Pietrinferni, A., Kowalski, P. M., & Isern, J. 2010, ApJ, 716, 1241
Salaris, M., Althaus, L. G., & García-Berro, E. 2013, A&A, 555, A96
Shaffer, N. R., & Starrett, C. E. 2020, Phys. Rev. E, 101, 053204
Shternin, P. S., & Yakovlev, D. G. 2006, Phys. Rev. D, 74, 043004
Siess, L. 2007, A&A, 476, 893
Spitzer, L., & Härm, R. 1953, Phys. Rev., 89, 977
Urpin, V. A., & Yakovlev, D. G. 1980, Sov. Astron., 24, 126
Ventura, J., & Potekhin, A. 2001, in The Neutron Star – Black Hole Connection, eds. C. Kouveliotou, J. Ventura, & E. van den Heuvel, NATO Sci. Seri. C: Math. Phys. Sci., 567, 393
Wetta, N., & Pain, J.-C. 2020, Phys. Rev. E, 102, 053209
Yakovlev, D. G. 1987, Sov. Astron., 31, 347
Yakovlev, D. G., & Urpin, V. A. 1980, Sov. Astron., 24, 303
Ziman, J. M. 1960, Electrons and Phonons (Oxford: Oxford University Press)

[2] http://www.ioffe.ru/astro/conduct/index.html